Chipping mechanisms in rotary-percussive drilling: Experimental insights into the role of the median crack as precursor of the dynamic fragmentation process.

Aising, J., Gerbaud, L. and Sellami, H.
Mines Paris, Paris, France

Senechal, P
Université de Pau et des Pays de l'Adour, E2S UPPA, CNRS, DMEX, Pau, France

Moonen, P.
Université de Pau et des Pays de l'Adour, E2S UPPA, CNRS, LFCR, Pau, France

Ugarte, I.
Drillco Tools S.A., Santiago, Chile

ABSTRACT: Understanding the mechanisms governing the production of large fragments during rotary-percussive drilling is critical to optimizing drilling efficiency. According to the prevailing theory, these fragments can only be produced during the unloading phase of indentations by the closure of a specific crack, named median crack. The experimental evidence for this argument mostly comes from quasi-static indentations in amorphous materials, such as soda-lime glass. However, this material drastically differs from typically drilled rocks, where the degree of heterogeneity, grain size, and initial defects may modify the chipping mechanism. To investigate the fragmentation mechanism in typically drilled rocks, dynamic indentation tests were conducted on limestone and granite. Results of high-speed camera observations revealed that chipping occurred during the loading phase in the granite, and through segmentation analyses of tomographic images, that the median crack was often absent. Moreover, in the limestone, a correlation between of the onset of a Hertzian cone above the median crack system and the change in rate of growth of the side cracks experimentally support that the chipping mechanism in these two rocks must be related to the expansion of the crushed zone in the loading phase. Therefore, the prevailing theory cannot be generalized to any rock type.

1. INTRODUCTION

Roto-percussive drilling is the preferred method for drilling medium to high-strength rock formations, such as those encountered in quarries, mining, and geothermal operations. In this method, a piston repeatedly impacts a drill bit equipped with multiple tungsten carbide inserts that come into direct contact with the rock (L. E. Chiang & Elías, 2008). The impact generates a stress wave that travels down the drill bit towards the rock. When the stress wave reaches the end of the drill bit, the inserts indent the rock, inducing highly localized stresses that create dust and fragments of various sizes (Reyes et al., 2015), which are then removed by drag through a high-velocity air flow (C. H. Song et al., 2014), ensuring that the rock surface is clean for the next impact. Using the minimal amount of energy in the impact to generate the maximum number of fragments is key to optimizing the Rate of Penetration (ROP) and reducing carbon emissions in the industry (Gilbert et al., 2010). In this regard, various

authors have noticed that the large fragments observed in both laboratory experiments and field tests are generated by the coalescence of two specific types of cracks, known as radial cracks and side cracks (also called lateral cracks). Fig. 1 shows the typical idealized crack types developed in brittle materials by indentation (Cook & Pharr, 1990). Although the formation of radial cracks due to tangential stresses is well understood and accepted for crystalline and amorphous materials (Cook & Pharr, 1990), both with and without confinement (Wu et al., 2021), the mechanism that generates the side cracks, and particularly the moment at which they occur, is still debated (Cook & Pharr, 1990; Saksala, 2011). The prevailing theory follows the work of Lawn et al. (Lawn & Swain, 1975), who, through quasi-static indentations on soda-lime glass and other brittle, amorphous materials, characterized and described the evolution of median cracks and side cracks, suggesting that the side cracks occurs as a consequence of the closure of the median crack during the unloading phase. In the same approach,

Chiang et al. (S. S. Chiang et al., 1982) through a plasticity cavity model, further substantiated the notion that side cracks occur during unloading.
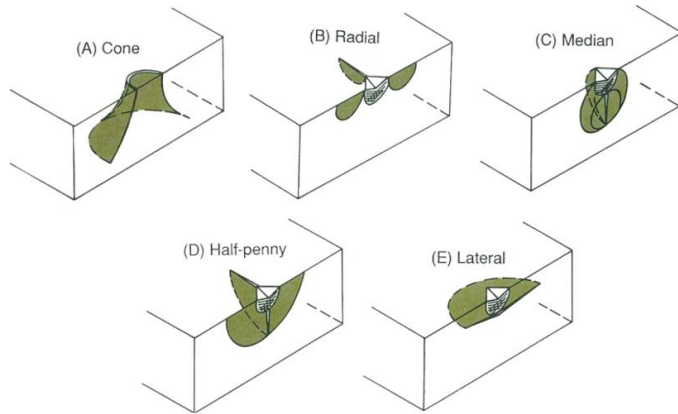

Fig. 1. Major cracks developed by indentations in brittle materials. (reprinted from Cook et al. 1990). (a) Cone crack (Hertzian cone), (b)Radial cracks, (c) Median cracks, (d) Half-penny crack, (e) Lateral cracks (also called side cracks).

Since then, various analytical and numerical studies have focused on understanding this mechanism. (Alehossein et al., 2000; Deng et al., 2020; Jiang et al., 2020; Lindqvist, 1984; Saadati et al., 2014; Saksala, 2011). Among these, Saksala (Saksala, 2011), simulating a particular case where the loading condition was adjusted to only obtain a Hertzian cone and side cracks, found that side cracks originate by bifurcating from the Hertzian cone during the unloading phase.

Contrary to the prevailing theory, other authors have reported experimentally, numerically, and analytically that in heterogeneous and crystalline materials, or amorphous materials with imperfections, side cracks are created during the loading phase rather than the unloading phase. Among these, Kou (Kou et al., 1977), using a cavity model, demonstrated that side cracks can nucleate during the loading phase from any pre-existing defect due to the volumetric expansion of the fractured zone. Liu (H. Y. Liu et al., 2008), analyzing the interaction between multiple inserts, found that very few acoustic emissions due to fragmentation occur during the unloading phase, and therefore, the side cracks must form during loading, attributing this to the heterogeneity and brittleness of the rock.

With evidence suggesting that side cracks can nucleate both during loading and unloading, the reason why the latter has been assumed as the general rule is not clear (Cook & Pharr, 1990). Wang (Wang et al., 2011) points to the difficulty and simplicity of early numerical models in correctly capturing the difference between homogeneous and heterogeneous materials, with weakness planes and initial defects. Consequently, such models may not adequately represent materials in which side cracks typically occur during loading. Cook (Cook & Pharr, 1990), in a comprehensive review of various

experiments, suggests that the widespread adoption of this sequence can be attributed to the fact that early experiments were predominantly conducted on amorphous and transparent materials, such as soda lime glass. These materials offered the advantage of enabling direct observation of the crack system through fractography. Consequently, the particular fracture scheme of these materials was then generalized to other types of materials. Furthermore, it is noteworthy that most of these experiments were conducted under quasi-static conditions, where the unloading phase is externally imposed to the indentation process. This stands in contrast to dynamic impact indentation, where the initiation of the unloading phase is the result of a self-driven and complex interaction process between the bit and the rock, further distinguishing it from quasi-static conditions.

While the discrepancy may seem trivial, it is indeed of utmost relevance, as from these experimental observations, analytical or numerical models are formulated or calibrated to predict behavior under conditions that, due to cost or physical limitations, cannot be replicated in controlled laboratory tests. (Kou et al., 2004).

In addition, the potential mischaracterization of the radial-median crack system from thin cross sections has also been also discussed in literature. Thin cross sections pose difficulties in distinguishing whether radial cracks extend towards the surface from a median crack or if they represent a distinct type of crack on their own (Cook & Pharr, 1990).

To overcome the limitations of characterizations from thin cross-sections, X-ray Computed Tomography (XCT) has become an increasingly employed technique for describing damage in geomaterials (Ghamgosar et al., 2015; K. Liu et al., 2019; Shariati et al., 2019; Wu et al., 2021). This technique allows for rapid inspection of the sample interior without the need for sectioning, thereby avoiding potential alterations. Moreover, the study of crack trajectories, roughness, propagation angles, and crack thickness is also feasible (Ju et al., 2020). Furthermore, through segmentation and deep learning techniques, it is possible to recognize and segment various types of fractures (Forquin & Ando, 2017; Ma et al., 2020; Okuma et al., 2022; Pham et al., 2023).

This work aims to highlight the differences in fragmentation between two types of rocks typically drilled by DTH hammers and contribute to clarifying some of the discrepancies described earlier. To achieve this, dynamic indentation tests were conducted over a wide range of impact velocities, covering those typical of DTH hammers. The timing of the appearance of side cracks on the surface of the rocks was determined using a high-speed camera. Through XCT and Deep Learning segmentation, the evolution of each of the main crack systems was characterized.

2. EXPERIMENTAL INVESTIGATION

2.1. Experimental setup

A gas-gun experimental setup was designed and built in the Mines Paris laboratories in Pau, France. The setup allows for the vertical fire of a piston onto a bit at speeds ranging from 4 to 14 m/s. Lower speeds can be achieved by free fall from 1.5 m. The bit features a single semi-spherical tungsten carbide insert with a diameter of 5/8". Light sensors determine the impact velocity and serve as triggers for recording the interaction between the bit and the rock with a high-speed camera. The frame rate allows for recording 12,000 frames per second with a resolution of 400x160 pixels. To apply WOB (Weight on Bit), four pneumatic cylinders can apply a preload on the bit of up to 150 kg. In terms of geometry, both the piston and the bit have circular cross-sections with diameters of 25 mm and 30 mm, respectively. The length of the bit is 265 mm, while the piston measures 260 mm. Both are made of steel with a density of 7850 kg/m^3. Fig. 2 shows an schematic representation of the experimental setup.
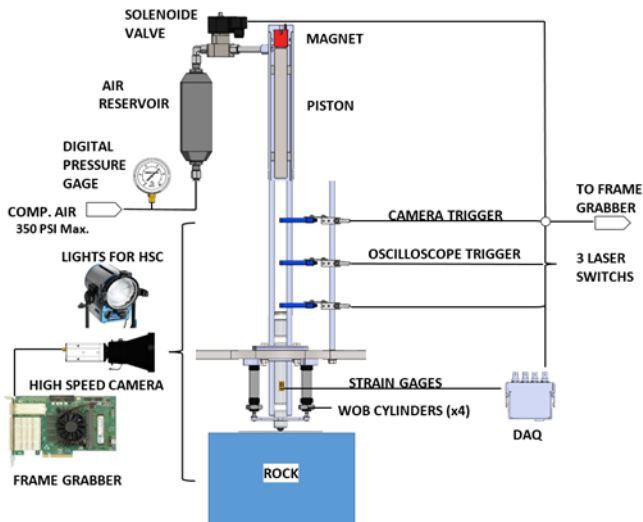

Fig. 2. Schematic representation of the experimental setup.

2.2. Rock properties

A Kuru grey granite (KG), extracted from quarries in Finland, and a Sainte Anne limestone (SA) from quarries in southern France were selected for the experiments. Kuru grey is characterized by its heterogeneity at the scale of the insert radius, meaning that the insert tip may come into contact with only one grain of a specific mineral (Aldannawy et al., 2021). The high level of interlocking between grains provides it with high tensile strength. On the other hand, Sainte Anne limestone is a homogeneous rock with numerous bioclastic inclusions (shells, corals) with some degree of metamorphism and a grain size smaller than 0.4 mm. The relevant mechanical properties are listed in Table 1. The samples used were hexagonal in shape, 25 cm in size. Up to eight impacts were performed on each sample. The centers of each impact were at least

5 cm apart from each other and from the free face. The height of the samples was kept between 13 and 15 cm. Fig. 3a and 3b depicts the shape of the rock samples and the arrangement of the impacts in the limestone and in the granite, respectively.

Table 1. Mechanical rock properties. Unconfined compressive strength UCS, Unconfined tensile strength UTS, density ρ, Elastic module E, porosity Φ, and Sound velocity V_s.

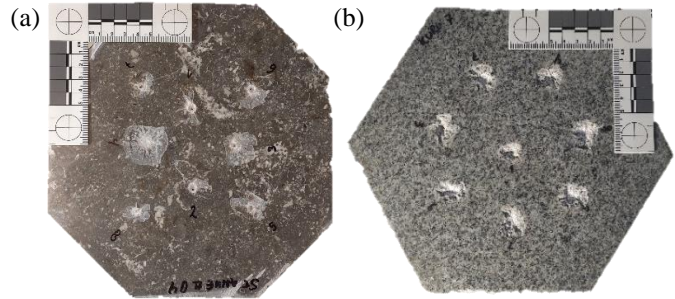| Rock	UCS (MPa)	UTS (MPa)	ρ (kg/m^3)	E (GPa)	Φ (%)	V_s (m/s)
SA	124	5.11	2692	70.6	0.7	5090
KG	192	12.5	2620	56.9	0.33	4646

Fig. 3. Final state of the rock surfaces after and debris removal. (a) Sainte Anne limestone, (b) Kuru grey granite.

2.3. X-ray computed tomography (XTC)

To characterize the internal damage, samples of 46 mm (limestone) and 65 mm (granite) in diameter were scanned at the DMEX Center for X-ray Imaging at Pau University (UPPA), Pau, France. X-ray Computed Tomography (XCT) is a non-destructive technique increasingly used in geosciences because it allows obtaining three-dimensional representations of internal features without the need to cut the sample into sections (Cnudde and Boone 2013, Saur et al. 2020, 2021), thus avoiding the alteration of cracks caused by the mechanical sectioning of samples. In XCT, the sample is placed between a source and a detector. During an acquisition, a conical X-ray beam traverses the sample and a series of 2D projection images are recorded for various sample orientations. The pixel values of each of these images correspond to the intensity of the transmitted X-ray beam and depend on the nature of the sample material, as expressed by the well-known Beer-Lambert law:

$$I = I_0 e^{-\mu h}$$

where I_0 is the incident X-ray intensity, I is the intensity remaining after the X-rays pass through a sample of thickness h and μ is the linear attenuation coefficient that is function of the density and the atomic number of the sample material.

To determine the optimal scanning conditions, initial tests were conducted using a Tescan UniTOM XL tomograph.

This instrument is equipped with a polychromatic 300 W X-ray source with a tunable energy level between 30 kVp and 180 kVp, and a 16 bit flat panel capable of acquiring images of 2856 x 2856 pixels. Regarding the resolution, three voxel sizes were tested (36, 26, and 15 µm). 26 µm was found to provide a good trade-off between field of view and resolution. The scans reported in this work were obtained using a 180 keV tube voltage, an effective target power of 26 W, a copper filter of 1.5 mm thickness, an exposure time of 3.5 s. For each scan, 2877 radiographs were acquired and used to reconstruct the 3D datasets, that were subsequently visualized and analysed using the specialized software Dragonfly (Object Research Systems Inc.).

2.4. Cracks segmentation by Deep learning

Image segmentation involves arranging the voxels (= pixels of the three-dimensional image) into different classes, each corresponding to a different material phase or feature. Various techniques exist, either based on the voxel values themselves, or their spatial variation. These conventional methods tend to perform poorly for crack detection, as they are generally blurry, poorly defined, and follow random patterns. (Pham et al., 2023). To overcome these issues, deep learning models have been successfully applied. These models enable significant improvements in detecting vaguely defined patterns by training a neural network. Among these, the U-Net model developed by Ronneberger (Ronneberger et al., 2015) has proven to be effective in a wide range of fields. In this work, a pre-designed U-Net architecture in Dragonfly was trained to segment the cracks present in the samples. While the detection of just cracks is possible (i.e., training the network to recognize a single class), we found that by training the network to recognize the matrix as a whole (e.g., quartz, biotite, and feldspars in the case of granite treated as a single class) surrounding the cracks helps to increase the percentage of accuracy in crack recognition. Although the segmentation of radial cracks from side cracks is theoretically feasible, the best results were obtained by training the network to recognize a single class where radial, side, and median cracks were treated as a single crack class.
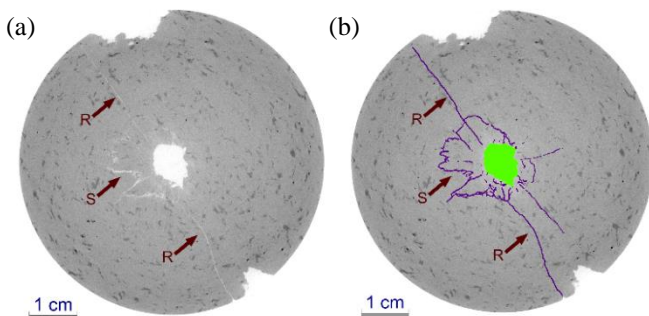
(a)   (b)

Fig. 4. Cross-sections of a Kuru granite sample (a) before and (b) after segmentation. Radial (R) and side (S) cracks are observed in purple. The crater is seen at the center in green.

Fig. 4a depicts a cross-sectional view perpendicular to the axis of indentation. Radial and lateral cracks (plus the crater in the central area) are clearly discernible. Fig. 4b shows the segmentation result, where radial cracks (R) are indistinguishable from side cracks (S). The crater was also segmented as its circular shape is easily recognizable by the U-Net model. For the sake of clarity, the matrix layer has been hidden.

3. RESULTS AND ANALYSES

3.1. Impact test on Sainte Anne limestone

The first impact sequence was carried out on Sainte Anne limestone. In this rock, a total of 14 impacts with impact velocities ranging from 2.5 to 12.84 m/s were conducted. Fig. 5 shows how the crater radius evolves as the impact velocity increases. A "staircase shape" can be observed, in which the crater radius does not increase within a range between 8 and 10 m/s. The same stepped shape was reported by Kou for different types of rocks (Kou et al., 1977) and subsequently analyzed numerically by Liu (H. Y. Liu et al., 2008). Although in their work the independent variable was the length of the side cracks and the dependent variable was the impact force, both are equivalent, respectively, to the crater radius and to the impact velocity: The crater radius is just the length of a side crack that emerged on the surface, while the dynamic force F is proportional to the impact velocity according to $F \cong 0.5\rho c v$, where ρ is the steel density, c the speed of sound, and v the impact speed. According to their numerical simulations, Liu argued that the zone where the length of the side cracks remains almost constant was due to the expansion of the fractured zone beneath the insert, causing the lateral cracks to nucleate from the fractured zone or diverge from a Hertzian cone.
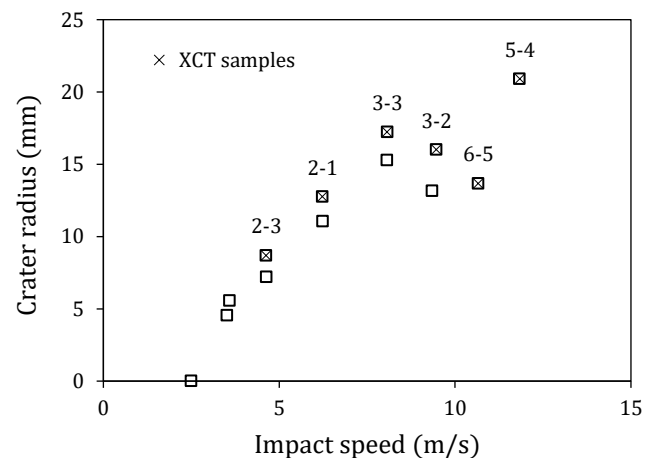

Fig. 5. Crater radius as a function of impact speed in Sainte Anne limestone. A staircase shape was observed in which the radius remains almost constant. The samples selected for analysis by XCT are the squares with the inner cross marker. The sample id is shown above the marker. XCT samples define the top of the trend.

To understand the mechanism that has generated this characteristic shape in Fig. 5, six core samples were extracted and analyzed using XCT, as detailed in sections 2.3 and 2.4. In Fig. 5, the selected samples have been identified with a cross marker. These selected samples define the upper part of the trend. Section 3.5 presents the analysis of the tomography data, revealing a notable evolution of the crack system beneath the fractured zone.

3.2. Impact test on Kuru grey granite

The second impact sequence was conducted on Kuru granite. Similar to limestone, impact velocities covered a wide range. However, the results presented in this study focus on a single impact velocity equal to 11 m/s, as most of the relevant observations regarding whether chipping occurs during loading or unloading, and whether the unique condition for side crack generation is the prior generation of a median crack beneath the insert can be observed with only this condition. Out of the total tests, six impacts were selected for analysis. Since the impact velocity was nearly the same for all six samples, the results—presented in Fig. 6—are presented as a function of the maximum indentation velocity of the bit. The bit indenting velocity was calculated from the penetration/time curve obtained by tracking the bit in high-speed videos.
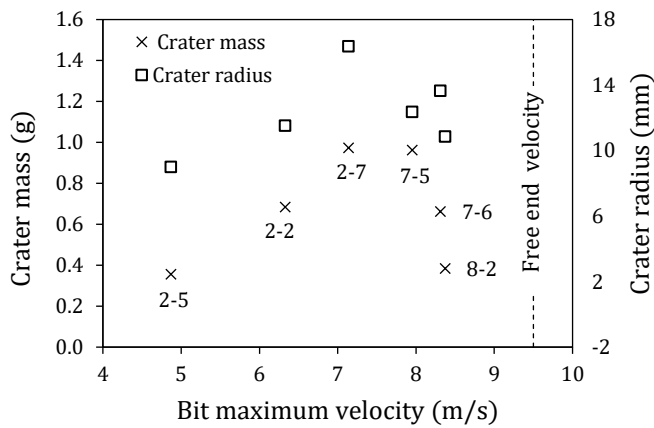

Fig. 6. Crater mass and Crater radius as a function of the bit maximum indenting velocity in Kuru grey granite. The sample id is shown close to the crater value.

Bit indentation velocity can be interpreted as a measure of the local rock penetration stiffness K. For instance, if the local rock stiffness is extremely high, i.e $K = \infty$, the bit indentation velocity will be null. At the opposite extreme, an extremely soft rock, i.e. $K = 0$, represents a free end condition, where the bit velocity will be approximately equal to the piston impact velocity. Considering the masses of the piston and the bit, and an average impact velocity of 11 m/s for the analyzed dataset, the maximum achievable velocity by the bit when $K = 0$ corresponds to 9.5 m/s. Such a limit condition is depicted in Fig. 6 as a vertical dashed line. From Fig. 6, it is clear that a trend

exists both for crater size and for the crater mass as a function of the bit indentation velocity. When the rock behaves locally rigidly, as in sample KG2-5, the mass removed is relatively low. As the local stiffness decreases, the mass removed increases up to a maximum—occurring at sample KG2-7—before dropping drastically as the local stiffness approaches that of a free end equivalent. The existence of a maximum as a function of the apparent rock stiffness of the rock has been widely reported and studied (Lundberg, 1973; X. Song et al., 2019; Wijk, 1989). Given that the impact energy was approximately equal for all tests, it is interesting to analyze whether there are any clues in the fracture pattern beneath the insert that allow understanding the observed trend. The observations made in this regard are addressed in Section 3.6.

3.3. Radial and median crack timing

From high-speed video recordings, the bit indentation curve could be reconstructed through tracking. Kinovea Software was used for this purpose. Direct observation of the moment of appearance of radial cracks and chipping on the sample surface allowed determining if these were formed during the unloading stage or not. Table 2 summarizes the observations for both rocks: The maximum bit indentation u_m, the time t_m at which the bit reaches u_m, the time t_1 at which radial cracks were observed, and the time t_2 at which the emergence of side cracks on the surface was observed. It is worth clarifying that u_m is not the crater depth. Here, we assume that the observed chipping corresponds to the emergence of side cracks on the surface. This assumption is supported by visually inspecting the length of the side cracks that almost reached the surface with the corresponding crater size (see Figs. 9 and 10).

Fig. 7 and 8 present the dimensionless indentation curves for the limestone and for the granite, respectively. In these figures, time and displacement have been scaled using the pair (t_m, u_m) listed in Table 2 as a reference.

Table 2. Radial and chipping timing

Rock	Test #	u_m (mm)	t_m (μs)	t_1 (μs)	t_2 (μs)
Sainte Anne	2-3	n/a	n/a	n/a	n/a
	2-1	0.65	225	225	392
	3-3	0.73	199	199	366
	3-2	0.92	197	197	364
	6-5	0.98	250	167	333
	5-4	1.12	250	167	250
Kuru grey	2-5	0.99	218	127	218
	2-2	1.54	454	91	181
	2-7	1.12	226	136	226
	7-5	1.65	386	136	220
	7-6	1.46	363	196	280
	8-2	2.05	363	113	196

The dimensionless time at which the appearance of a radial crack or chipping on the surface was detected is overlaid on each of the curves. With this notation, it is evident that for $t/t_m < 1$ a fracture was detected during loading, while for, $t/t_m > 1$, it was detected during unloading.

For limestone (see Fig. 7), all the radial cracks were obtained practically at the end of the loading stage, while all side cracks were observed during unloading, consistent with Lawn's general model and with the fragmentation sequence of amorphous "anomalous" materials (Cook & Pharr, 1990).
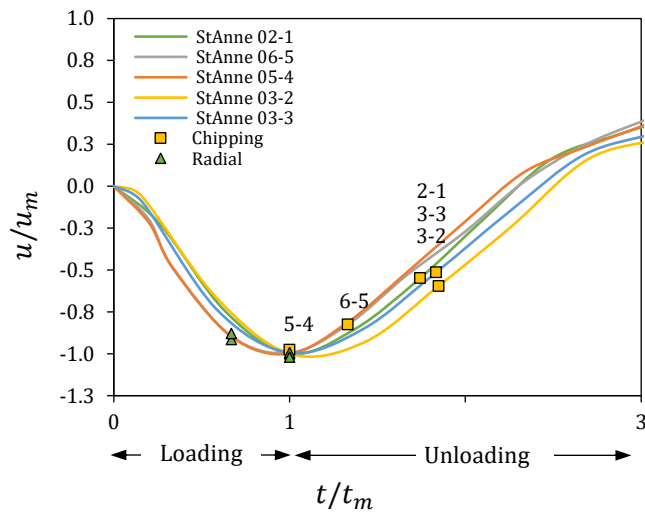

Fig. 7. Adimensional time displacement curve. Sainte Anne limestone. Square markers indicate the time at which chipping was detected. Triangle indicate the timing at which radial cracks were detected.
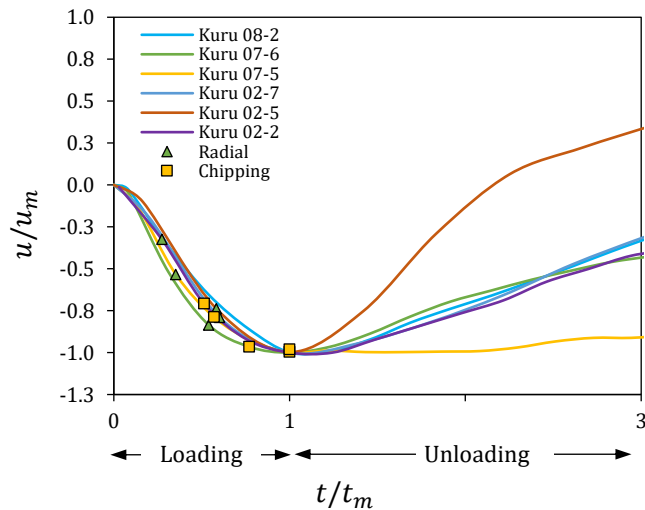

Fig. 8. Adimensional time displacement curve. Kuru grey granite. Square markers indicate the time at which chipping was detected. Triangle indicate the timing at which radial cracks were detected.

More specifically, at impact velocities under 10 m/s, the appearance of side cracks on the surface was observed

towards the end of unloading. A trend to advance the appearance of fragments towards the beginning of unloading phase was observed as the impact velocity was increased from 10 m/s to 12 m/s.

For Kuru granite (see Fig. 8) both radial and side cracks were observed during the loading stage. Radial cracks originate very early during indentation, consistent with what has been described by Cook et al. for crystalline materials (Cook & Pharr, 1990). The detection of chipping during the loading phase has at least two consequences. First, it is axiomatic that the fracture mechanism cannot be due to the closure of the median crack during unloading; otherwise, chipping would obviously be observed during unloading. Second, there is a possibility that the median crack may not even have formed during the indentations. The second point will be analyzed in detail in Section 3.6.
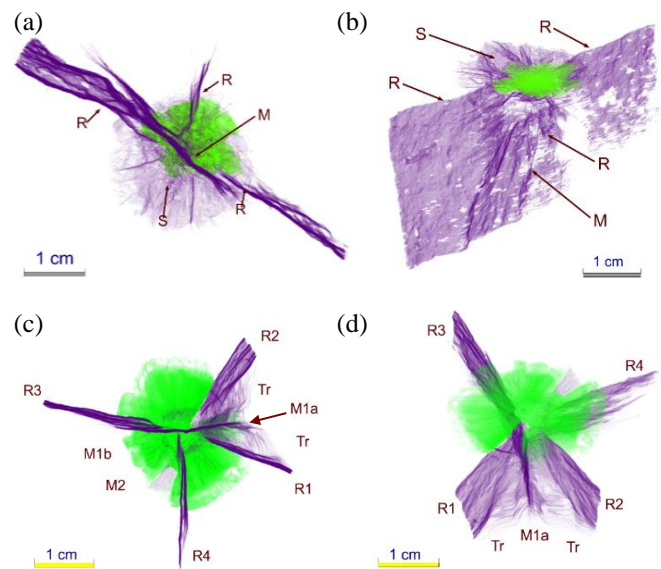

Fig. 9. 3D representation of the crack systems. (a) Bottom view of a Kuru granite. (b) 3D pictorial view clearly showing the coalescence of the median and the radial crack. (c) Bottom view of the limestone. (d) 3D view

3.4. Observations on the radial crack system.
Although the nucleation of radial cracks due to hoop stresses is fully understood, some small discrepancies may still be observed in the way the propagation of these cracks is described: In some idealized schemes, these are described as 'the extension of medium cracks to the surface' (Lindqvist, 1984), implying that these cracks can only exist if a medium crack has been previously developed. Alternatively, this system is also referred to in the literature as a 'half-penny' crack system (see Fig. 1). Fig. 9 contains examples of segmentations applied to a granite sample and a limestone sample. The first column shows a bottom view to highlight the cracks rather than the crater, while the second column shows 3D views at a chosen viewing angle to highlight each of the different

cracks. In the case of the granite, Fig. 9a, a single median crack can be observed. This has propagated from below the insert within a vertical plane containing the impact axis. It is possible to observe that the plane from which the two radial cracks have been formed does not coincide with the plane containing the median crack, elucidating that in this rock the radial cracks are a different crack system from that of the median crack, and not traces on the surface of the median crack. This is even more evident in the limestone. In this, it is possible to observe a main median crack, labeled M1 in Fig 9c, with a gentle kink right at the vertical axis. A part of the crack, labeled M1a, lies between two radial cracks R1 and R2. Interestingly, both radial cracks coalesce with the main crack M1a through a transition crack (Tr). The existence of this transition crack is conclusive evidence that both cracks were generated from different locations, and as they propagated, they became merged. The same is true in the opposite direction: a radial crack R3 coalesces with a part of the median crack labeled M1b, although the transition is less evident.

3.5. Tomographic analysis of Sainte Anne limestone

Fig. 10 shows the result of the segmentations performed as described in Section 2.4. Examining the sequence of images in the "Bottom view" column, it can be observed that at the lowest impact velocities, only radial cracks and side cracks appear. Although the crater has formed due to side cracks (S), the absence of traces of the median crack (M) suggest that the mechanism that promote the nucleation of side cracks at low impact velocities does not depend on the occurrence of the median crack. In sample SA2-1, it is already possible to observe a well-defined system of median cracks. Apparently, there is a main median crack (M1) from which a secondary median crack (M2) has propagated perpendicular to it. It is interesting to note how two radial cracks, R1 and R2, generated on totally different planes from that of M1, deflect towards M1, creating a transitional crack (Tr). In sample SA3-3, which defines the onset of the transition in crater growth rate in the Fig. 5, a significant alteration in the characteristic shape of the median crack is observed in the "Top view" column. The crack exhibits a prismatic (P) shape symmetrically aligned with the indentation axis. Due to its acute propagation angle, it is evident that this crack does not conform to a Hertzian cone, but rather corresponds to the propagation pattern of four median cracks. Additionally, a lateral crack (also referred as deep lateral cracks) initiated between radial cracks R3 and R2. Referring to sample SA3-2, the first to show a slight decrease in crater size, the appearance of a typical Hertzian cone (H) is observed. The cone angle, measured from the vertical, is equal to 18°, which remained practically unchanged in the other samples (see the "Side view" column). The independence of the Hertzian cone angle from the indenter diameter and load—and its sole dependence on the Poisson's ratio—has been previously observed in glasses by Roesler (Roesler, 1956). The kink of the Hertzian cone between 5 and 7 mm below the surface appears, according to Marimuthu (Marimuthu et al., 2016), due to a change in the stress field at the crack tip caused by an over-indentation. From the side view, it is also possible to observe a lateral crack (L), which has bifurcated from the skirt of the Hertzian cone, exactly as Liu has postulated. The side cracks (also called shallow lateral cracks) remain unable to propagate to the surface, probably due to the extra energy consumption in the formation of the Hertzian cone.

Remarkably, we found a characteristic not foreseen by the numerical analysis of Liu, likely due to the inability of the model to accurately depict variations in 3D crack systems: The transition in the characteristic propagation pattern of the median crack system. In this instance, the system of median cracks has conformed to a star-like configuration, with three median cracks (M1 to M3) propagating equidistantly at 120° from the axis of indentation. In sample SA6-5, this configuration shifts back to a prismatic (P) configuration with four median cracks, akin to sample SA3-3. However, unlike in SA3-3, the creation of the Hertzian cone in SA6-5 has required greater energy consumption, compromising crater extension. Finally, in sample SA5-4, both the Hertzian cone and the median crack have fully stabilized, as no changes in their surface extension could be noticed. Consequently, the increased amount of energy available due to the higher impact velocity was used to extend the side cracks to the surface, elucidating the subsequent increase in crater diameter.

3.6. Tomographic analysis of Kuru granite

Fig. 11 shows the results of the tomographic analysis and segmentation conducted on the Kuru granite samples. It is worth noting here that all these samples were impacted with the same impact velocity, so any variation observed in the fragmentation patterns arise from the rock itself, as a result of the inherent heterogeneity of this type of rock.

Referring to the third column "bottom view" in Fig. 11, it can be noticed that out of the six samples analyzed, only sample KG2-5 formed a well-defined median crack. We believe it is not a coincidence that this sample exhibited the least damage along with the lowest indentation velocity of the bit. It is plausible that the median crack developed only in this sample due to the high apparent local stiffness of the rock. Across the remaining samples, the common characteristic is the complete absence of the median crack. Only in sample KG2-7, which represent the "optimum" in this series of impacts, there is a crack resembling a median crack. However, a thorough inspection reveals that what appears to be a median crack is actually the coalescence of two radial cracks that have propagated beneath the fractured area. The same kind of coalescence of two radial cracks as has also been reported by Cook et al. (Cook & Pharr, 1990).

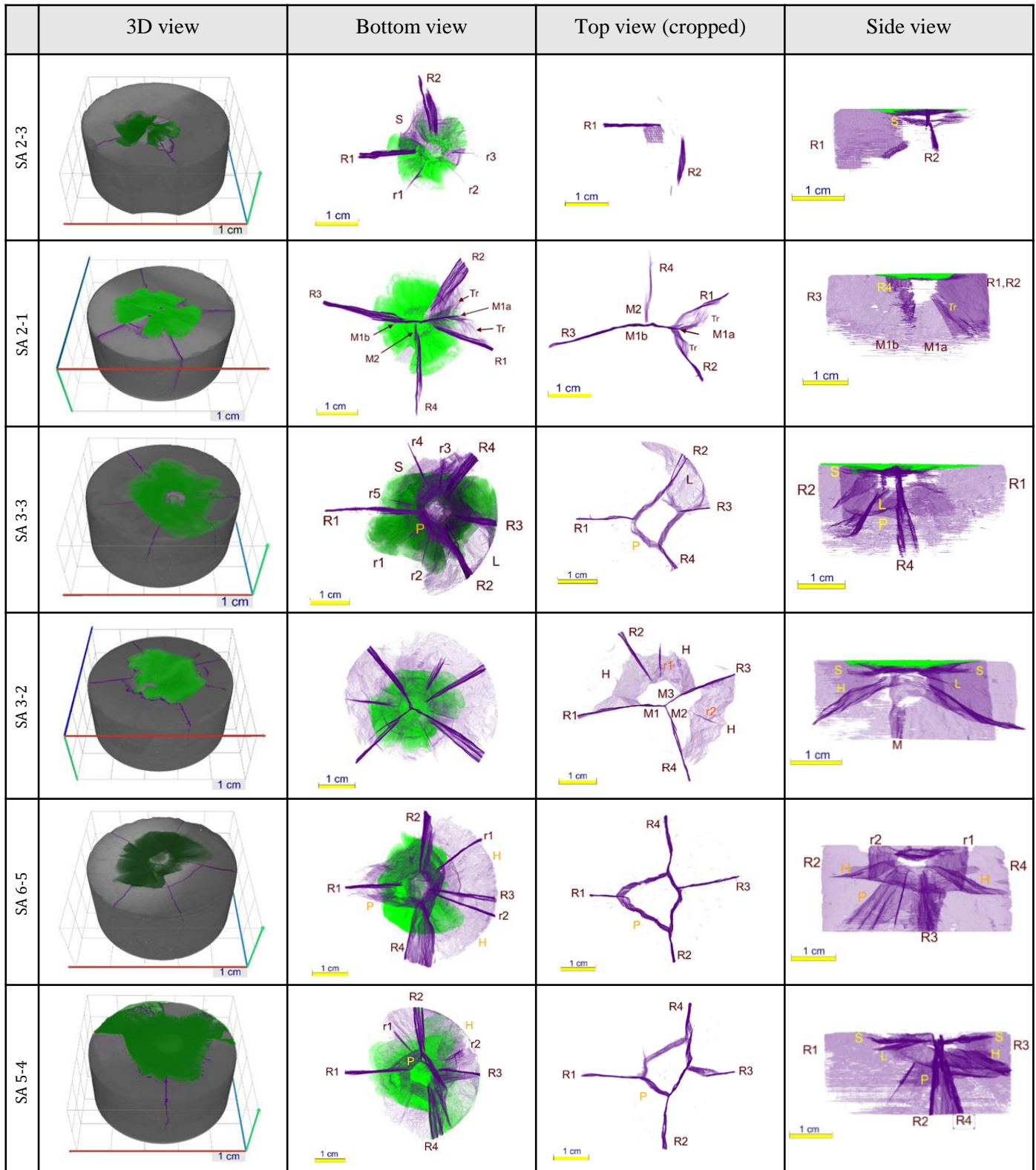|	3D view	Bottom view	Top view (cropped)	Side view
SA 2-3				
SA 2-1				
SA 3-3				
SA 3-2				
SA 6-5				
SA 5-4				

Fig. 10. Fractures patterns in Sainte Anne limestone. First column 1: 3D view. Second column: Bottom view. Third column: Top view cropped to highlight median crack system instead of the crater. Four column: Side view. Rows organized from top to bottom according to impact velocity, from lowest to highest.

Referring now to samples KG7-5, KG7-6, and KG8-2, corresponding to the decreasing part in Fig. 6, a notable decrease in radial crack generation was observed, being non-existent in sample KG8-2. The same trend can be observed for the side cracks. In summary, when the apparent rock stiffness tended to behave like a free end, the rock's ability to propagate cracks notably decreased. Yet, a well-defined, albeit smaller, crater was obtained.
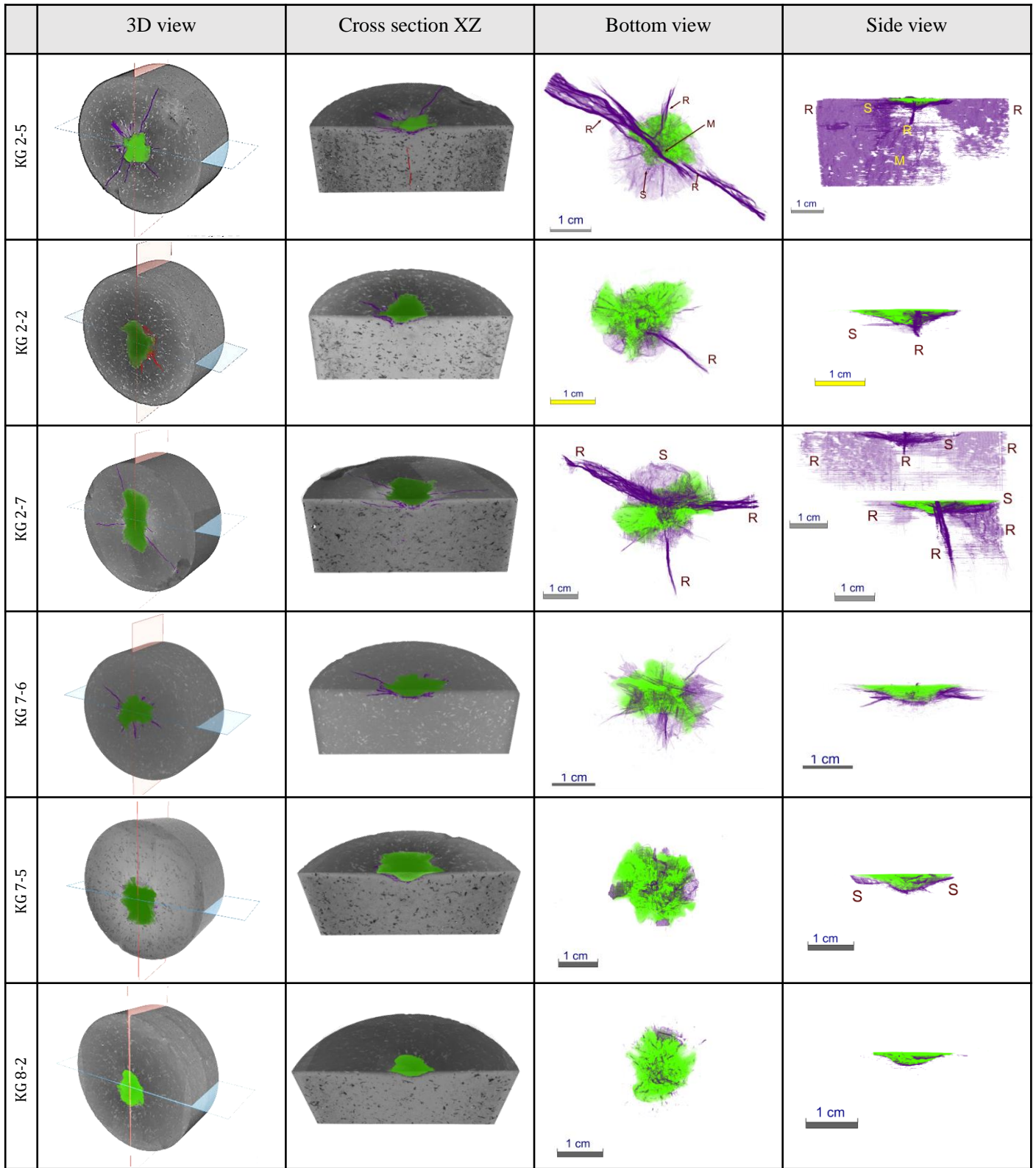
Fig. 11. Fractures patterns in Kuru granite. First column 1: 3D view. Second column: Cross section in XZ plane (blue plane in the 3D view). Third column: Bottom view. Four column: Side view. Rows organized from top to bottom according bit indenting velocity, from lowest to highest.

The absence of the median crack system in the majority of the samples analyzed, linked to the observation of fragmentation during loading, reveals that the fragmentation mechanism in granitic rocks, often with internal defects, must be related to the volumetric expansion of the fractured zone, a hypothesis postulated by Liu et al. through numerical simulations, although without experimental evidence to support it.

4. CONCLUSIONS

This study has provided a highly detailed characterization of dynamic impacts in two rock types. These have served as a basis for further understanding of the mechanism that leads to large fragments in rotary-percussive drilling, and which are crucial for increasing the efficiency of these tools. The use of a high-speed camera has made it possible to assess when the fragments were generated during unloading, following the prevailing theory, or when they were generated during loading.

From dimensionless indentation curves we have shown that in limestone radial cracks were formed late during loading. For Kuru granite, radial cracks formed early during loading, like most crystalline materials. Surprisingly, side cracks were always observed during loading, or at most, just at the end of loading.

Using X-ray computed tomography, the subsurface cracks of the samples were analyzed. We revealed that in the limestone the occurrence of a Hertzian cone precisely coincides with the starting point of the transition where the diameter of the crater remains almost constant, thus experimentally validating hypotheses that have been proposed numerically. It was also found that in this type of rock, the median crack propagated in specific patterns according to the dynamic load applied. At low impact velocities no median cracks were observed, but fragmentation does occur, thus indicating that the generation of fragments is not univocally related to the presence of a median crack. At higher impact velocities, the median crack evolved in complex arrangements ranging between two, three and four cracks. In the case of four median cracks, we found that they adopted a prismatic shape, where each side of the prism was a median crack. Regarding the granite, it was shown that the median crack was often absent.

The provided evidence as a whole suggests that the fragmentation sequence proposed by Lawn and ascribed by other authors is far from being generalizable. The evident differences between the two rocks implicate that the fragmentation mechanism is characteristic to each rock, and depends more on the properties and characteristics of each rock rather than on the loading conditions.

Finally, further evidence has been provided to elucidate that the radial cracks are, by themselves, a crack system independent of the median cracks, and not traces of the median cracks on the surface.

Future research and collaborations using numerical tools that can accurately represent the behaviors described herein should be the next steps towards a better understanding of dynamical fragmentation.

REFERENCES

Aldannawy, H. A., Gerbaud, L., & Rouabhi, A. (2021). On the influence of tool shape on percussive drilling in hard rocks. *55th U.S. Rock Mechanics / Geomechanics Symposium 2021*, *1*, 517–526.

Alehossein, H., Detournay, E., & Huang, H. (2000). An analytical model for the indentation of rocks by blunt tools. *Rock Mechanics and Rock Engineering*, *33*(4), 267–284. https://doi.org/10.1007/s006030070003

Chiang, L. E., & Elías, D. A. (2008). A 3D FEM methodology for simulating the impact in rock-drilling hammers. *International Journal of Rock Mechanics and Mining Sciences*, *45*(5), 701–711. https://doi.org/10.1016/j.ijrmms.2007.08.001

Chiang, S. S., Marshall, D. B., & Evans, A. G. (1982). The response of solids to elastic/plastic indentation. I. Stresses and residual stresses. *Journal of Applied Physics*, *53*(1), 298–311. https://doi.org/10.1063/1.329930

Cnudde, V, Boone, M. (2013). High-resolution X-ray computed tomography in geosciences: a review of the current technology and applications. *Earth-Sceince Reviews*. 123, 1–17. doi: 10.1016/j.earscirev.2013.04.003.

Cook, R. F., & Pharr, G. M. (1990). Direct Observation and Analysis of Indentation Cracking in Glasses and Ceramics. *Journal of the American Ceramic Society*, *73*(4), 787–817. https://doi.org/10.1111/j.1151-2916.1990.tb05119.x

Deng, Y., Yin, F., Deng, H., Li, J., & Liu, W. (2020). Research on crack propagation and rock fragmentation efficiency under spherical tooth dynamic indentation. *Arabian Journal of Geosciences*, *13*(2). https://doi.org/10.1007/s12517-019-4926-7

Forquin, P., & Ando, E. (2017). Application of microtomography and image analysis to the quantification of fragmentation in ceramics after impact loading. *Philosophical Transactions of the Royal Society A: Mathematical, Physical and Engineering Sciences*, *375*(2085). https://doi.org/10.1098/rsta.2016.0166

Ghamgosar, M., Stewart, P., & Erarslan, N. (2015). Investigation the effect of cyclic loading on fracture propagation in rocks by using Computed Tomography (CT) techniques. *49th US Rock Mechanics / Geomechanics Symposium 2015*, *4*, 2851–2855.

Gilbert, Y., Hagström, M., & Getliff, J. M. (2010). Reducing the carbon footprint of drilling and completion operations. *Society of Petroleum Engineers - SPE International Conference on Health, Safety and Environment in Oil and Gas Exploration and Production 2010*, *2*(April), 1280–1294. https://doi.org/10.2118/126756-ms

Jiang, H., Cai, Z., Wang, O., & Meng, D. (2020). Experimental and Numerical Investigation of Hard Rock Breakage by Indenter Impact. *Shock and Vibration*, *2020*. https://doi.org/10.1155/2020/2747830

Ju, M., Li, J., Li, J., & Zhao, J. (2020). Loading rate effects on anisotropy and crack propagation of weak bedding plane-rich rocks. *Engineering Fracture Mechanics*, *230*(February), 106983. https://doi.org/10.1016/j.engfracmech.2020.106983

Kou, S. Q., Liu, H. Y., Lindqvist, P.-A., & Tang, C. A. (2004).

Rock fragmentation mechanisms induced by a drill bit. *International Journal of Rock Mechanics and Mining Sciences*, *41*(3), 460. https://doi.org/10.1016/j.ijrmms.2003.12.127

Kou, S. Q., Xiangchun, T., & Lindqvist, P. A. (1977). Modelling of excavation depth and fractures in rock caused by tool indentation. In *Report R-99-11, Lulea University of Technology, 1977.*

Lawn, B. R., & Swain, M. V. (1975). Microfracture beneath point indentations in brittle solids. *Journal of Materials Science*, *10*(1), 113–122. https://doi.org/10.1007/BF00541038

Lindqvist, P. A. (1984). Stress fields and subsurface crack propagation of single and multiple rock indentation and disc cutting. *Rock Mechanics and Rock Engineering*, *17*(2), 97–112. https://doi.org/10.1007/BF01042712

Liu, H. Y., Kou, S. Q., & Lindqvist, P. A. (2008). Numerical Studies on Bit-Rock Fragmentation Mechanisms. *International Journal of Geomechanics*, *8*(1), 45–67. https://doi.org/10.1061/(asce)1532-3641(2008)8:1(45)

Liu, K., Zhang, Q. B., Wu, G., Li, J. C., & Zhao, J. (2019). Dynamic Mechanical and Fracture Behaviour of Sandstone Under Multiaxial Loads Using a Triaxial Hopkinson Bar. *Rock Mechanics and Rock Engineering*, *52*(7), 2175–2195. https://doi.org/10.1007/s00603-018-1691-y

Lundberg, B. (1973). Energy transfer in percussive rock destruction-II. Supplement on hammer drilling. *International Journal of Rock Mechanics and Mining Sciences And*, *10*(5), 401–419. https://doi.org/10.1016/0148-9062(73)90025-9

Ma, X., Kittikunakorn, N., Sorman, B., Xi, H., Chen, A., Marsh, M., Mongeau, A., Piché, N., Williams, R. O., & Skomski, D. (2020). Application of Deep Learning Convolutional Neural Networks for Internal Tablet Defect Detection: High Accuracy, Throughput, and Adaptability. *Journal of Pharmaceutical Sciences*, *109*(4), 1547–1557. https://doi.org/10.1016/j.xphs.2020.01.014

Marimuthu, K. P., Rickhey, F., Lee, H., & Lee, J. H. (2016). Spherical indentation cracking in brittle materials: An XFEM study. *Proceedings of 2016 7th International Conference on Mechanical and Aerospace Engineering, ICMAE 2016*, 267–273. https://doi.org/10.1109/ICMAE.2016.7549548

Okuma, G., Maeda, K., Yoshida, S., Takeuchi, A., & Wakai, F. (2022). Morphology of subsurface cracks in glass-ceramics induced by Vickers indentation observed by synchrotron X-ray multiscale tomography. *Scientific Reports*, *12*(1), 1–10. https://doi.org/10.1038/s41598-022-11084-0

Pham, C., Zhuang, L., Yeom, S., & Shin, H. S. (2023). Automatic fracture characterization in CT images of rocks using an ensemble deep learning approach. *International Journal of Rock Mechanics and Mining Sciences*, *170*(June), 105531. https://doi.org/10.1016/j.ijrmms.2023.105531

Reyes et al. (2015). Cuttings Analysis for Rotary Drilling Penetration Mechanisms and Performance Evaluation. *49th US Rock Mechanics / Geomechanics Symposium*, *2*(June), 1498–1505.

Roesler, F. C. (1956). Brittle Fractures near Equilibrium. *Proceedings of the Physical Society. Section B*, *69*(10),

981–992. https://doi.org/10.1088/0370-1301/69/10/303

Ronneberger, O., Fischer, P., & Brox, T. (2015). U-Net: Convolutional Networks for Biomedical Image Segmentation. *Lecture Notes in Computer Science (Including Subseries Lecture Notes in Artificial Intelligence and Lecture Notes in Bioinformatics)*, *9351*(Cvd), 234–241. https://doi.org/10.1007/978-3-319-24574-4_28

Saadati, M., Forquin, P., Weddfelt, K., Larsson, P. L., & Hild, F. (2014). Granite rock fragmentation at percussive drilling - experimental and numerical investigation. *International Journal for Numerical and Analytical Methods in Geomechanics*, *38*(8), 828–843. https://doi.org/10.1002/nag.2235

Saksala, T. (2011). Numerical modelling of bit–rock fracture mechanisms in percussive drilling with a continuum approach. *International Journal for Numerical and Analytical Methods in Geomechanics*, *30*(35), 1483–1505. https://doi.org/10.1002/nag.974

Saur, H., Sénéchal, P., Boiron, T., Aubourg, C., Derluyn, H., Moonen, P. (2020). First investigation of quartz and calcite shape fabrics in strained shales by means of X-ray tomography, *Journal of Structural Geology*, 130, https://doi.org/10.1016/j.jsg.2019.103905

Saur, H., Moonen, P., Aubourg, C. (2021). Grain fabric heterogeneity in strained shales: insights from XCT measurements, *JGR Solid Earth*, 126(9), e2021JB022025. doi: 10.1029/2021JB022025

Shariati, H., Saadati, M., Bouterf, A., Weddfelt, K., Larsson, P. L., & Hild, F. (2019). On the Inelastic Mechanical Behavior of Granite: Study Based on Quasi-oedometric and Indentation Tests. *Rock Mechanics and Rock Engineering*, *52*(3), 645–657. https://doi.org/10.1007/s00603-018-1646-3

Song, C. H., Kwon, K. B., Park, J. Y., Oh, J. Y., Lee, S., Shin, D. Y., & Cho, J. W. (2014). Optimum design of the internal flushing channel of a drill bit using RSM and CFD simulation. *International Journal of Precision Engineering and Manufacturing*, *15*(6), 1041–1050. https://doi.org/10.1007/s12541-014-0434-6

Song, X., Kane, A., Aamo, O., & Detournay, E. (2019). A dynamic model of the drilling action of percussive tools. *53rd U.S. Rock Mechanics/Geomechanics Symposium. American Rock Mechanics Association (ARMA)*, *September*.

Wang, S. Y., Sloan, W., Liu, H. Y., & Tang, C. A. (2011). Numerical simulation of the rock fragmentation process induced by two drill bits subjected to static and dynamic (impact) loading. *Rock Mechanics and Rock Engineering*, *44*(3), 317–332. https://doi.org/10.1007/s00603-010-0123-4

Wijk, G. (1989). The stamp test for rock drillability classification. *International Journal of Rock Mechanics and Mining Sciences And*, *26*(1), 37–44. https://doi.org/10.1016/0148-9062(89)90523-8

Wu, G., Liu, K., Hu, W. R., Li, J. C., Dehkhoda, S., & Zhang, Q. B. (2021). Quantification of dynamic damage and breakage in granite under confined indentation. *International Journal of Rock Mechanics and Mining Sciences*, *144*(January). https://doi.org/10.1016/j.ijrmms.2021.104763